PLANETARY SCIENCE

The development of lower-atmosphere turbulence early in a solar flare

N. L. S. Jeffrey*, L. Fletcher, N. Labrosse, P. J. A. Simões

We present the first observational study of the onset and evolution of solar flare turbulence in the lower solar atmosphere on an unprecedented time scale of 1.7 s using the Interface Region Imaging Spectrograph observing plasma at a temperature of 80,000 K. At this time resolution, nonthermal spectral line broadening, indicating turbulent velocity fluctuations, precedes the flare onset at this temperature and is coincident with net blue-shifts. The broadening decreases as the flare brightens and then oscillates with a period of ~10 s. These observations are consistent with turbulence in the lower solar atmosphere at the flare onset, heating that region as it dissipates. This challenges the current view of energy release and transport in the standard solar flare model, suggesting that turbulence partly heats the lower atmosphere.

INTRODUCTION

Solar flares are the marked result of magnetic energy release and dissipation in the Sun's atmosphere. This energy release and transfer is initiated by magnetic reconnection in the solar corona, but how it proceeds is still actively debated. During and following reconnection, random motions of the magnetized plasma—magnetohydrodynamic (MHD) plasma turbulence—may play a vital role in converting magnetic energy to the kinetic energy of accelerated particles and heating the flare corona to temperatures over 10 million kelvin (MK) (1). In the standard solar flare model, the energy from this remote energy release site in the corona is then transported by particles alone to heat the lower solar atmosphere. However, turbulent energy may also be dissipated and heat multiple regions throughout the flaring atmosphere (2), from the corona to the chromosphere (3).

The shape of an emitted spectral line can be used to understand the velocity distribution of the emitting particles. Early flare studies using full-Sun x-ray spectroscopy found that, during the early phase of some flares, spectral lines from >10-MK plasma exhibited linewidths in excess of what is expected from random thermal motions alone (4, 5), the so-called nonthermal line broadening. While line broadening can be caused by other mechanisms, such as opacity or pressure broadening, these should be negligible in optically thin solar flare plasma (6). The excess line broadening is thought to result from the superposed Doppler-shifted emission of turbulent fluid motions.

Spatially resolved observations with the Hinode (7) extreme ultraviolet imaging spectrometer (EIS) (8) have greatly increased our knowledge of the role turbulence plays during a flare. Significant nonthermal broadening is found in solar active regions, even in the preflare stages (9). In flares, Doschek et al. (10) found that nonthermal broadening increased with temperature and height in the coronal loop top source. Another study showed that the nonthermal broadening of one line, formed at 16 MK in the corona, peaked before the acceleration of electrons in the "impulsive" phase of the flare (11). Further, the ratio of the turbulent kinetic energy to accelerated electron power gave a time scale for dissipating this turbulence of 1 to 10 s, similar to predictions of MHD models (12). These studies provide convincing observational evidence that MHD turbulence can act as a key energy transfer intermediary in the corona, heating plasma and converting magnetic energy into the kinetic energy of flare-accelerated electrons.

Large line broadening (~100 km/s) resulting from this turbulence is not unexpected in high-temperature regions close to coronal sites of flare energy release. However, do turbulent velocity fluctuations exist in the lower atmosphere, as well as the corona, during a flare? The Interface Region Imaging Spectrograph (IRIS) (13) permits the detailed study of flares in the chromosphere and the transition region (the thin atmospheric layer connecting the corona to the chromosphere). Both EIS and IRIS have observed nonthermal broadenings of over 50 km/s, in lines emitted in the heated lower flaring atmosphere, at temperatures ranging from 10,000 K to 10 MK (6, 14). However, as they are often accompanied by "chromospheric evaporation" (15, 16), which is a net up-flow of expanding lower-atmosphere plasma heated to well over 1 MK, disentangling turbulence and unresolved flows in this expansion can be difficult, particularly from data with low temporal resolution.

To investigate turbulent velocity fluctuations before and at the flare onset, before significant energy deposition and heating, we need to observe the rapid initial flare evolution at as high a temporal resolution as possible. Using IRIS data, we report the first high time resolution spectroscopic study of early flare turbulence in the lower solar atmosphere. The observation captures this flare with an unprecedented 1.7-s time resolution and a high spatial resolution of 0.33″ (~240 km).

RESULTS

We observe a B-class flare (SOL2016-12-06T10:36:58) in active region 12615 (fig. S1). Our analysis covers the flare from preflare to decay. Two bright flare ribbons, a signature of energy dissipation in the lower atmosphere, are observed in the extreme ultraviolet at 131 Å from the Solar Dynamics Observatory (SDO) Atmospheric Imaging Assembly (AIA) (17) during the impulsive phase. The Reuven Ramaty High Energy Solar Spectroscopic Imager (RHESSI) (18) observes x-ray emission up to 9 keV. Integrating over a 4-min period shows a 6- to 12-keV source located close to the western ribbon (Fig. 1).

The temporal evolution of one spectral line, Si IV 1402.77 Å (laboratory wavelength), formed at ~80,000 K (see Materials and methods and fig. S2), is examined. We study the period between 10:36:51 UT (universal time; +870 s from the IRIS start time of 10:22:22 UT) and 10:39:02 UT (+1000 s). During this time, the IRIS slit sits over the eastern flare ribbon, moving <1″ in the east-west direction, so that it observes essentially the same location at all times presented here. Having determined that Si IV is optically thin (see Materials and methods), we analyze the line using single Gaussian line fitting and a nonparametric

School of Physics and Astronomy, University of Glasgow, G12 8QQ Glasgow, UK.
*Corresponding author. Email: natasha.jeffrey@glasgow.ac.uk
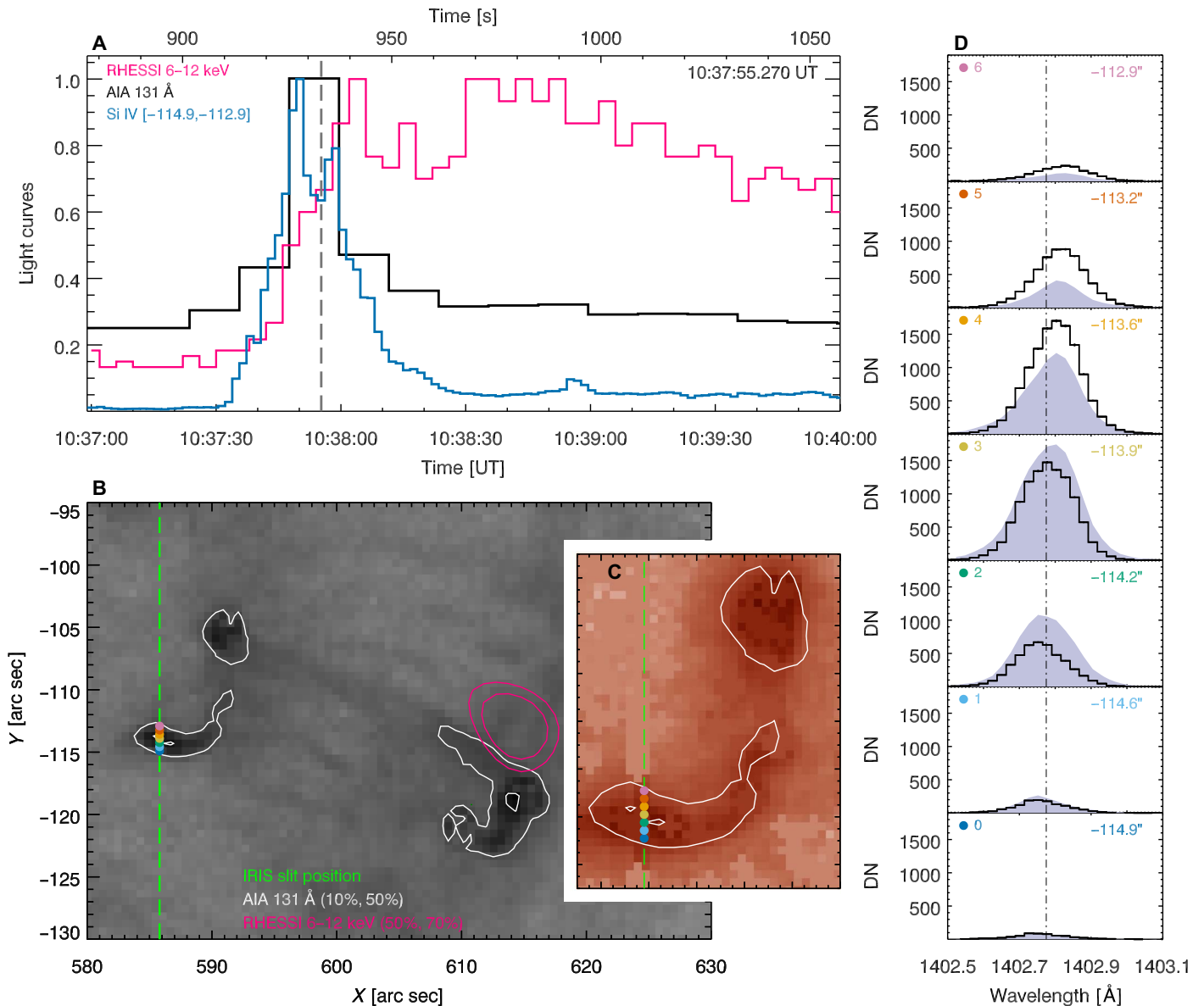
Fig. 1. Light curves and the images and line spectra of flare SOL2016-12-06T10:36:58 at 10:37:55 UT. (**A**) Si IV 1402.77 Å (blue), RHESSI 6 to 12 keV (pink), and AIA 131 Å (black) light curves. (**B**) AIA 131 Å background image with contours (white) showing the IRIS slit position (green) and RHESSI 6 to 12 keV contours (pink). (**C**) The eastern ribbon using an IRIS slit-jaw 1400 Å image overlaid with AIA 131 Å contours. (**D**) Si IV spectral lines at seven locations [colored dots in (B) and (C)]; black line, current time; violet solid, previous time. The dashed-dotted line shows the position of the inferred reference wavelength of 1402.775 ± 0.020 Å. A movie showing all times is available (movie S1). DN, data number.

moment analysis to determine the emitting plasma motions. We measure the line centroid positions, giving the bulk flow velocities v, relative to an inferred reference wavelength of 1402.775 ± 0.020 Å, with an uncertainty corresponding to ±~4 km/s (see Materials and Methods). The width of the line is determined as a Gaussian full width at half maximum (FWHM).

Figure 2 shows the example spectral lines and their Gaussian fits at six times, while Fig. 3 shows the temporal evolution of the centroid positions (bulk flow velocities v) and widths (nonthermal motions v_{nth}), for a spatially integrated region covering 2″ in the north-south direction, alongside the Si IV integrated intensity and RHESSI 6- to 12-keV x-ray light curve. The nonthermal width of Si IV begins to

increase at 900 s, well before the Si IV intensity starts to rise. It peaks at 910 s, cotemporal with the start of the rise of Si IV intensity. Expressed as the nonthermal velocity, the linewidth increases from a preflare level of $v_{nth} \approx 9$ km/s to a peak of $v_{nth} \approx 30$ km/s at 910 s, with the line intensity peaking 20 s later, at 930 s. By 940 s, when the RHESSI 6- to 12-keV emission first peaks, v_{nth} has returned to preflare levels.

During the peak phase, v_{nth} displays periodic variations, which can be fitted with a sinusoidal function, estimating period $P \approx 11.5$ s and amplitude $A \approx 3.4$ km/s. In the 30 s prior to the rapid rise in v_{nth} at the start of the flare, the line wavelength is systematically blue-shifted. From the onset of the rapid rise in v_{nth} at 900 s, this blue-shift increases
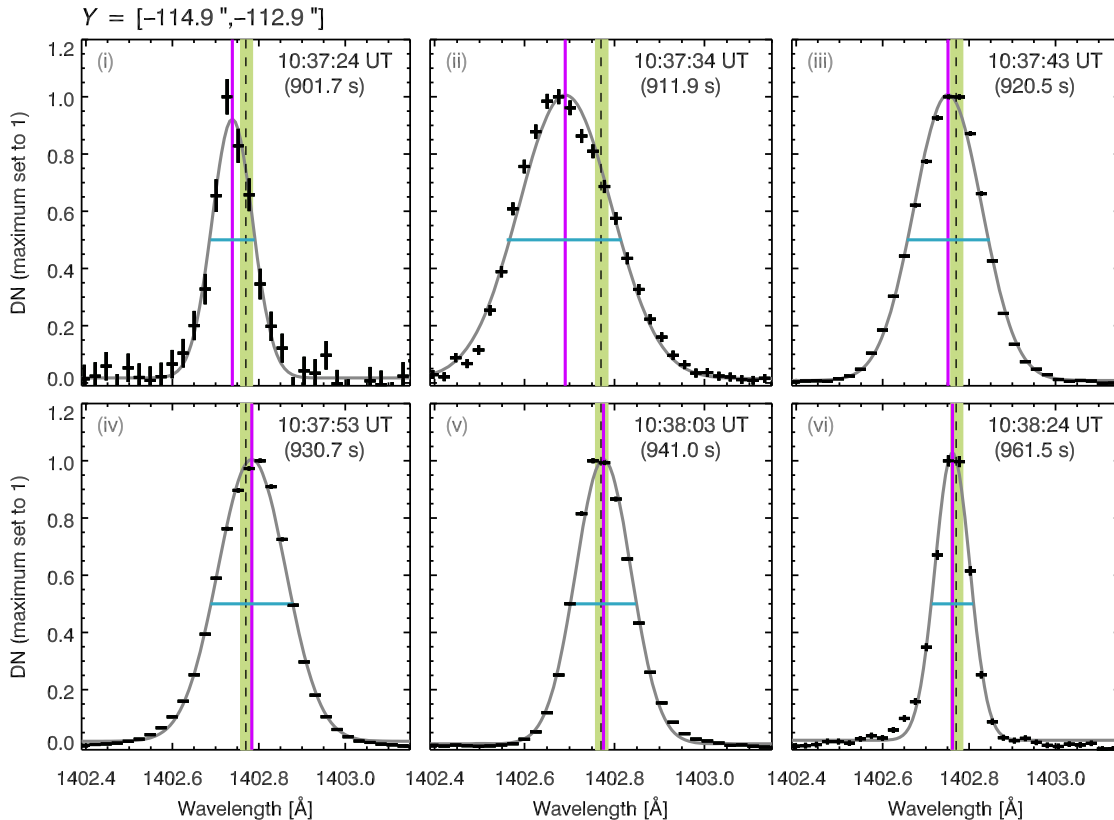
Fig. 2. Temporal evolution of Si IV spectral lines during the flare. The Si IV lines at six example flare times (black), observed over a 2″ region along the north-south direction. The lines are fitted with a single Gaussian (gray) that provides an estimate of the line centroid position (vertical purple line) and FWHM (horizontal turquoise line). We show the inferred Si IV reference wavelength plus its uncertainty (1402.775 ± 0.020 Å) (lime regions) and the Si IV laboratory wavelength (1402.77 Å) (black dashed lines).
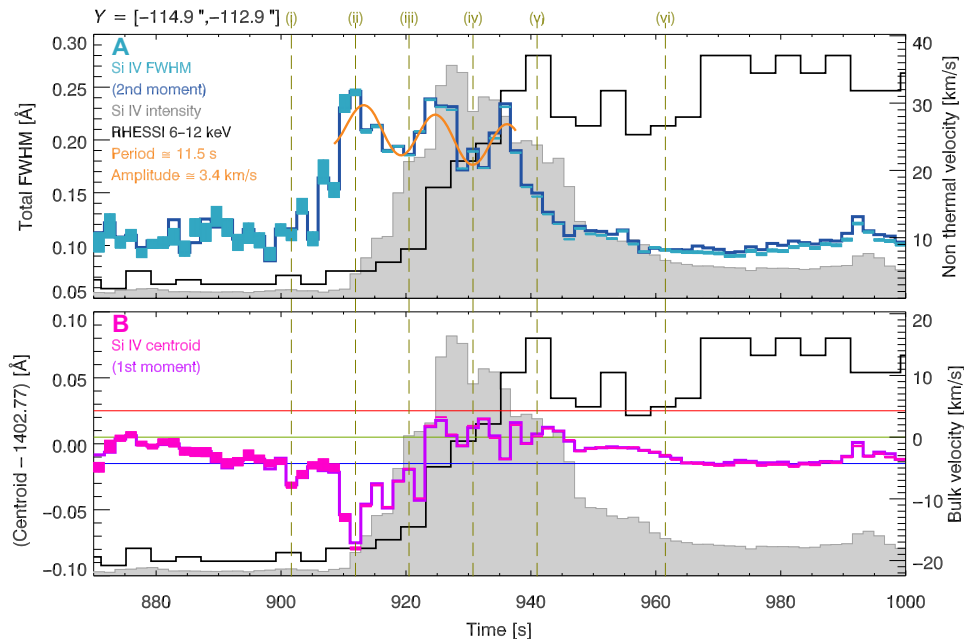
Fig. 3. Temporal evolution of the Si IV line properties during the flare. (**A**) The total FWHMs and nonthermal velocities v_{nth} (turquoise) and (**B**) the centroid positions and bulk velocities v (purple), observed over a 2″ region along the north-south direction. Both the results of the Gaussian fitting and the moment analysis (see legend) give near-identical results. The Si IV integrated intensity (gray) and the RHESSI 6- to 12-keV light curve (black) are displayed. The dashed lines indicate the times of six spectral lines shown in Fig. 2. Top: A sinusoidal function is fitted to the variations in v_{nth}, estimating the period P and amplitude A (see legend). Bottom: Inferred reference wavelength (lime) and uncertainty (red and blue).
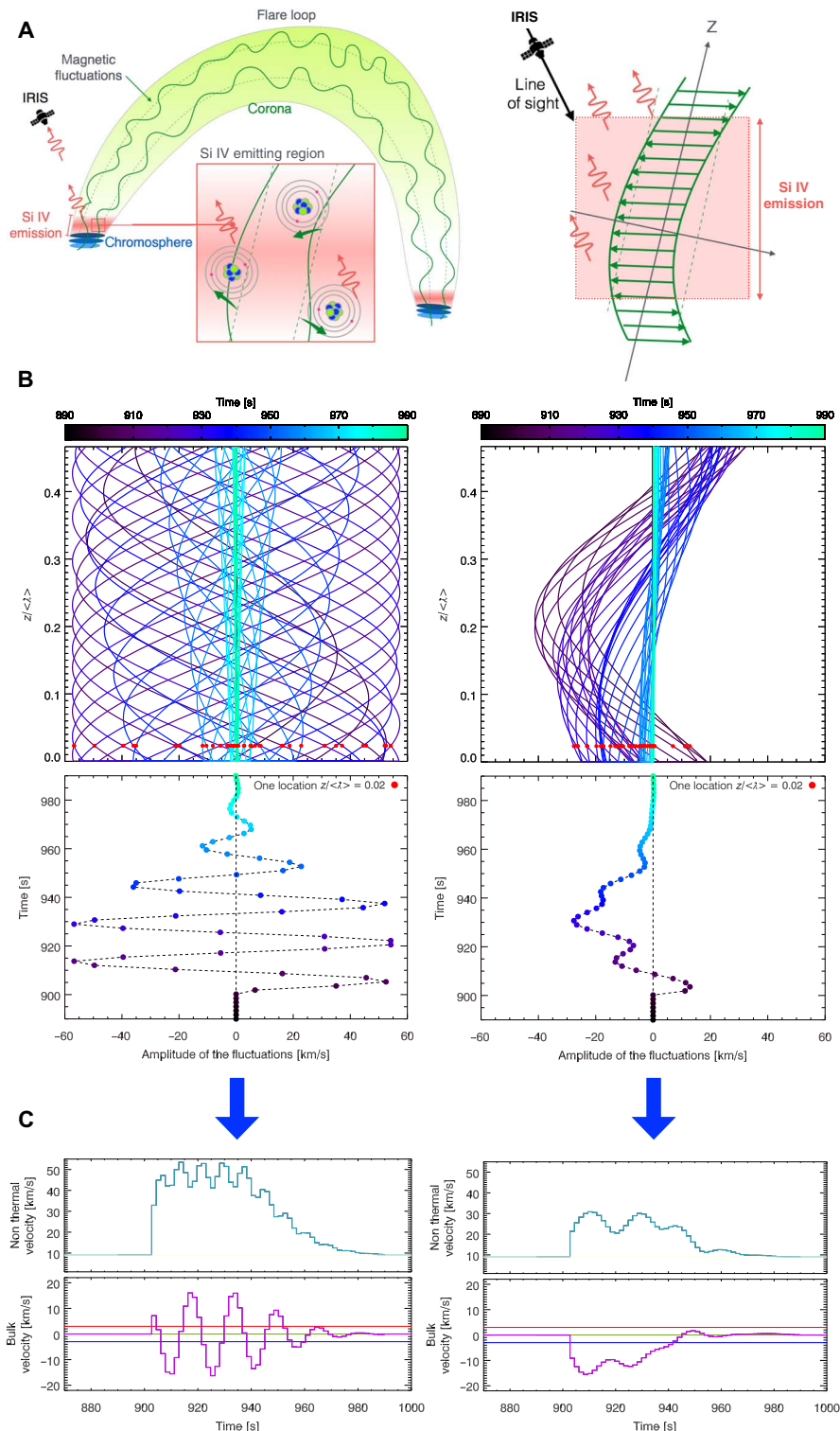
Fig. 4. A cartoon of the flaring loop and an interpretation of the observations. (**A**) We envisage a situation where multiple velocity fluctuations occur in the coronal loop and in the region emitting Si IV (red) before and during the flare, perpendicular to some guiding field direction z, and at some angle >0° to the line of sight. (**B**) Left: We set up a wave and pass it through the modeled region, along z, representing the region emitting Si IV. As the wave passes the length of the region (denoted as $z/\langle\lambda\rangle$, where $\langle\lambda\rangle$ is the average wavelength of the wave), its amplitude and wavelength vary with time. (**C**) Left: An observer (i.e., IRIS) sees all motions (velocity fluctuations) integrated along the line of sight, and we determine the resulting bulk velocity (first moment) and nonthermal velocity (second moment). One wave with varying amplitude and wavelength cannot reproduce the IRIS observations; a single wave produces clear oscillations in the bulk velocity. (B, right) – as (B, left) but for a spectrum of 10 different interacting waves (here, representing wave interactions that can lead to turbulent dissipation). This produces a result (C, right) similar to the IRIS observation, helping us to understand the nature of plasma fluctuations in the emission region (see Materials and Methods). Movies for (B) are available (movies S2 and S3).

rapidly over the next 10 s to −18 km/s, stopping abruptly as v_{nth} reaches its first peak. The blue-shift then decreases, taking the line centroid back to its reference wavelength.

DISCUSSION

Our interpretation is as follows. First, the evolution of the line intensity, nonthermal linewidth, and line centroid position provides evidence that turbulent velocity fluctuations are present in the lower solar atmosphere before the flare, contributing to plasma heating. The 30 km/s line broadening precedes the flare onset, as indicated by its impulsive radiation signatures observed in x-rays and (extreme) ultraviolet (although we cannot rule out gentle heating between 900 and 920 s). The Si IV intensity only begins to increase, indicating lower atmospheric heating, as the broadening reaches its peak, consistent with the idea that the dissipation of turbulent energy over ~10 s contributes to the heating of this region during the flare. The presence of turbulent signatures over ~60 s means that the driver of turbulence persists for longer. Si IV emission in flares is usually well correlated with flare hard x-rays (HXRs) (19), which provide the most direct signature of intense energy deposition by flare-accelerated electrons in the lower atmosphere. In this flare, however, there is no detectable high-energy HXR emission, although the 6- to 12-keV x-rays rise rapidly as the Si IV intensity peaks, possibly indicating low-energy nonthermal electrons.

Second, after its initial growth, the periodic variations of ~10 s in the line broadening are consistent with the growth and decay of a spectrum of interacting waves (turbulent velocity fluctuations) viewed over a spatially integrated region along the line of sight (see Fig. 4 and Materials and Methods). Because of instrumental constraints in previous missions, these rapid changes in broadening during a flare have not been observed previously [quasi-periodic oscillations have previously been observed in Si IV intensity and velocity (20), but on periods of minutes]. The growth, variation, and decay of the broadening coincide with movements in the Si IV centroid position, indicating small line-shifts, most notably a blue-shift of 18 km/s, cotemporal with the initial rise of v_{nth}. Since they occur before the intensity has reached its peak and decrease as the flare intensity increases, these shifts are unlikely to be due to chromospheric evaporation. However, the observed patterns of v_{nth} and v can both be produced simultaneously by modeling the passage of turbulent velocity fluctuations in the region. The passage of a single fluctuation (or wave) moving through a region, with varying properties (e.g., amplitude and wavelength), cannot reproduce the observed temporal patterns in v_{nth} and v, since this would produce a clear oscillation in the bulk velocity v (Fig. 4), but a spectrum of interacting fluctuations can reproduce the observation results (Fig. 4 and Materials and Methods). The spectral line Mg II 2796 Å, formed at lower temperatures, shows a similar bulk velocity pattern in the flare region, but with smaller blue-shifts of only 2 to 3 km/s (see Materials and Methods and fig. S3), possibly due to decreasing fluctuations at lower altitudes. Modeling these fluctuations also suggests that the size of the region emitting Si IV along the line of sight is comparable to the mean wavelength of the fluctuations (see Fig. 4 and Materials and Methods).

High time resolution measurements of the nonthermal and bulk velocities together provide detailed information about the nature of solar flare turbulence that can be compared with modeling, and emphasize the need for missions capable of subsecond spectroscopy. The results challenge the common view about the initiation of solar flares and our understanding of energy release and transport in astrophysical plasmas. This first report of rapid oscillatory behavior in the line broadening of Si IV in the flaring lower atmosphere is consistent with anisotropic plasma motions in the lower atmosphere becoming isotropic as the flare progresses (see Fig. 4 and Materials and
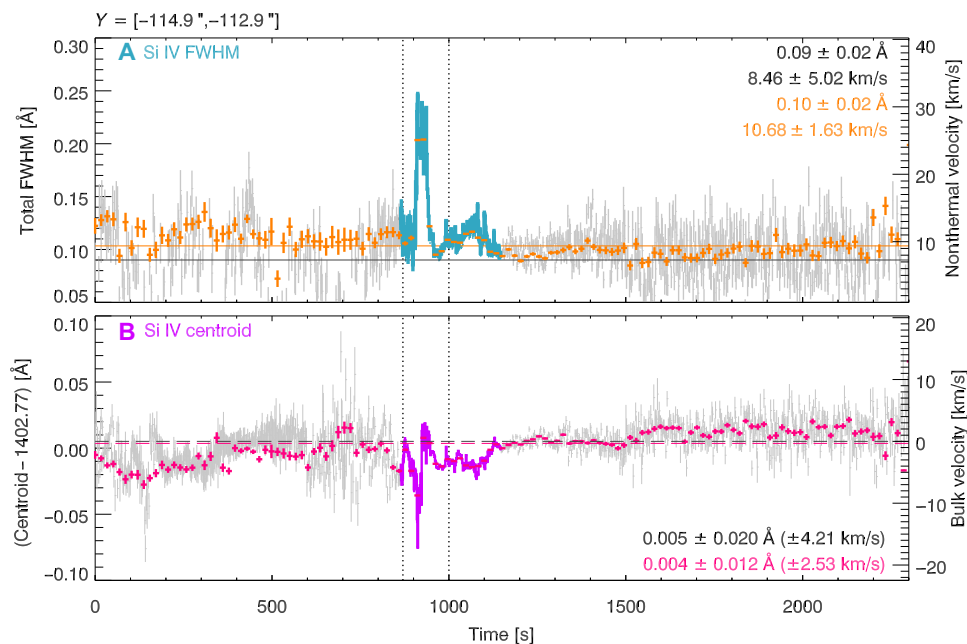
Fig. 5. Temporal evolution of Si IV 1402.77 Å. (**A**) FWHM (nonthermal velocity, v_{nth}) and (**B**) centroid position (bulk velocity, v) over the spatially integrated region of Y between −114.9″ and −112.9″ for all times observed by IRIS during the observation (gray) and the flare time [turquoise (A) and purple (B)]. In (A), the nonthermal velocity in the region before and after the flare is shown in the legend, calculated for the raster time resolution (black) and a time binned case (orange). In (B), the determined Si IV reference wavelength in the region plus its uncertainty is shown in the legend for the raster time resolution (black) and a time binned case (pink).
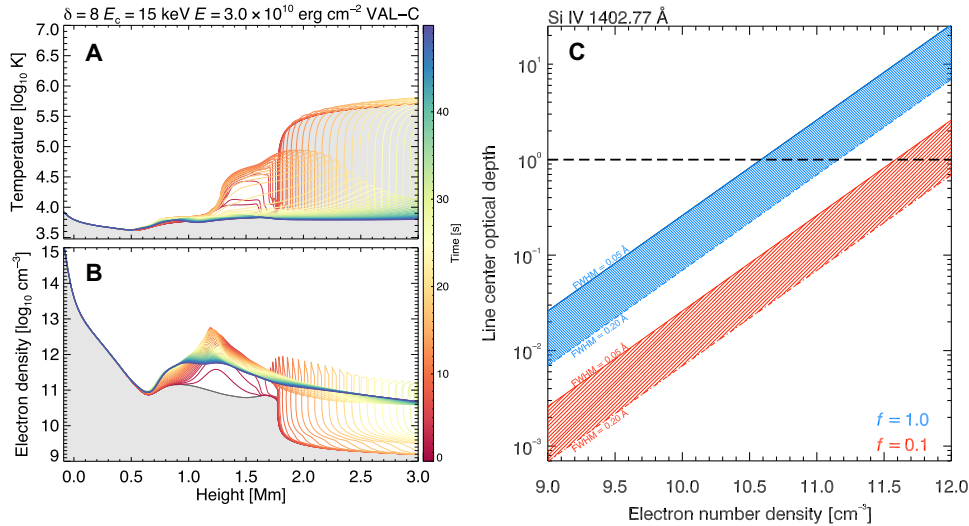
Fig. 6. Determining Si IV 1402.77 Å line optical depth. (A and B) An output from the RADYN simulations showing the flare model temperature (A) and electron number density (B) versus height above the photosphere, produced using the input parameters shown. The gray region shows the quiet Sun model atmosphere [VAL-C; (34)]. Si IV is formed at log T = 4.9, and the simulations indicate that the electron number density at this temperature ranges from log n_e = 9.5 to 11.5, particularly at early times. **(C)** The line center optical depth, determined using $\tau_0 \sim 0.26\, f\, <n_e>/10^{10}$ (cm^{-3}), versus electron number density n_e for different line FWHM and filling factors f. For most cases, Si IV 1402.77 Å should be optically thin (i.e., $\tau_0 < 1$) and free of radiative absorption effects.

Methods) and strongly implies that the turbulent dissipation of magnetic energy might occur throughout the flare loop, far from the flare energy release sites in the corona, just before and during the flare onset.

MATERIALS AND METHODS
IRIS observation of Si IV 1402.77 Å
IRIS is a space-borne ultraviolet spectrograph that provides high-resolution spectroscopy in three wavelength ranges of 1332 to 1358 Å, 1389 to 1407 Å, and 2783 to 2834 Å. It also provides slit-jaw imaging at four bands (C II 1330 Å, Si IV 1400 Å, Mg II k 2796 Å, and Mg II wing 2830 Å). During the studied observation, the position of the IRIS slit only moved an angular distance of ~7″ (~5000 km), from solar east to west, in ~1 hour. The IRIS raster used a rapid exposure time of 0.5 s, a slit movement time of ~1.7 s, and a field of view of 7″ × 128″. The pixel size in the north-south direction (along the Y axis) was 0.33″ (~240 km). For the data analysis, we used prepped level 2 IRIS data, and we removed any cosmic ray spikes. The data were then analyzed using the Interactive Data Language and Solar SoftWare (SSW) routine iris_getwindata.pro. We studied the strong line of Si IV 1402.77 Å (laboratory wavelength), which has no blends, and it was formed at the transition region temperature T(K) of log T = 4.9 (80,000 K, peak formation temperature; see fig. S2).

Between the flare times of ~10:37 and 10:40 UT, the IRIS slit only moved a small east-west distance of $X < 1″$, so we can study emission from approximately the same location at the start of the flare. We analyzed the first three moments of the Si IV 1402.77 Å line distribution using (i) a nonparametric moment analysis that calculates the line distribution integrated intensity (I; zero moment), centroid (λ_0; first moment), and variance (σ; second moment) using

$$I = \sum_{i=1}^{N} I_i, \;\; \lambda_0 = \frac{\sum_{i=1}^{N} I_i \lambda_i}{I}, \;\; \sigma = \frac{\sum_{i=1}^{N} I_i (\lambda_i - \lambda_0)^2}{I}$$

where λ denotes the wavelength (Å), and (ii) single Gaussian line fitting

$$I_i = A[0] + A[1]\exp\left(-\frac{(\lambda_i - A[2])^2}{2A[3]^2}\right)$$

where A[j] are the fitted parameters. Unlike other flare studies, where the determination of line shape was a key part of the analysis (21), here a detailed shape analysis was not required. We were only interested in an estimate of the random plasma motions along the line of sight (e.g., the second moment) and their temporal evolution. Hence, we approximated the entire line shape using a single Gaussian, even if the profile consists of multiple components. Since the number of line components is unknown and the fitting of multiple Gaussians is not well constrained, it is sensible to estimate the velocity of all random turbulent motions together using a single Gaussian in this study. This was compared with the values determined from the moment analysis, but we found that both studies produced near-identical results (Fig. 3 and fig. S4).

Determining a reference wavelength for Si IV 1402.77 Å
For the determination of the line centroid velocity (or bulk velocity v), we required a reference wavelength that determines the average Si IV wavelength observed by IRIS in "quiet" nonflaring regions during the observation. This is not necessarily the same as the Si IV 1402.77 Å laboratory wavelength provided by the CHIANTI line list (22, 23), but the reference wavelength acts as a zero point for the calculation of the line centroid velocities in this observation. Often, a reference wavelength for Si IV 1402.77 Å can be determined using photospheric lines with negligible flows, but none were suitable for determining a reference wavelength during this observation. Next, we attempted to determine a reference wavelength by obtaining the centroid position of Si IV 1402.77 Å from a region of "quiet Sun."

However, we also found that the Si IV 1402.77 Å signal was very low and barely above the background noise in regions away from the flare, even with a large north-south Y binning of ~50″. Last, since IRIS observes the active region for a time of approximately 1 hour, we calculated the average centroid position of Si IV 1402.77 Å over all observation times excluding the time of the flare between 10:37 and 10:40 UT, in our studied region, close to the flare, using a Y binning of 10″. From this, we determined a reference wavelength value of 1402.775 ± 0.020 Å (Fig. 5), which is very close to the laboratory wavelength. All the Si IV line centroid velocities in Figs. 2, 3, and 5 and figs. S3 and S4 are found relative to this reference wavelength. Converted to a velocity (km/s), the reference wavelength uncertainty is ±~4 km/s. Many studies find an average Si IV red-shift of 5 to 10 km/s in active regions (24), but we did not see any evidence of a red-shift here.

Optical depth of Si IV 1402.77 Å

In certain environments, Si IV 1402.77 Å might suffer from radiative absorption effects. For example, self-absorption features have been observed in Si IV lines during transient brightenings (25). Hence, we tested whether Si IV is likely to be optically thin for this study. If available, the Si IV 1393.76 Å/1402.77 Å doublet can be used to check the optical depth (26). Unfortunately, the Si IV 1393.76 Å line is not available in this observation. Therefore, we made an estimate of the optical depth τ using $\tau(\lambda) = \tau_0(\lambda_0) \Phi(\lambda)$ (27), where $\tau_0(\lambda_0)$ is the optical depth at the line center, λ_0 (Å) is the line centroid wavelength, and $\Phi(\lambda)$ is the absorption profile. Absorption effects are larger at the line center, and hence, we only calculated the optical depth at the line center using $\tau_0 \sim 0.26 f \langle n_e \rangle / 10^{10}$ (cm^{-3}), where f is a filling factor and n_e is the ionized electron number density (cm^{-3}).

Next, we used the radiative hydrodynamics code RADYN (28, 29) to model the possible flare atmospheric properties and to estimate the electron density n_e, where Si IV could be formed. To estimate the hydrodynamic response of the atmosphere and its properties such as temperature and electron number density, RADYN requires an input energy flux $(erg\ s^{-1}\ cm^{-2})$ that is usually estimated from the electron beam parameters determined from RHESSI x-ray analysis. We attempted to perform an analysis of the RHESSI spectral data for this flare. However, the low RHESSI sensitivity for this flare, the low count rate, and the small detectable energy range made the spectral analysis challenging. Nevertheless, sensible nonthermal electron parameters were estimated, and the resulting RADYN inputs and outputs are shown in Fig. 6. Here, we used model 84 from the F-CHROMA flare model database. Model 84 was chosen since it is based on a weak and soft nonthermal electron beam that is appropriate for this flare. The RADYN results suggest that, at early times, Si IV is likely formed over a large range of electron number densities of $\log n_e = 9$ to 12. Plugging these values into $\tau_0 \sim 0.26 f \langle n_e \rangle / 10^{10}$ (cm^{-3}) provides an optical depth τ_0 in the range of 0.0007 to 20.0 (Fig. 6). We also used the filling factor (f) values of 0.1 and 1.0 and the line-width (FWHM) between the thermal width of 0.05 and 0.2 Å, since τ_0 is inversely proportional to the FWHM. Figure 6 shows that for $\log n_e < 10$, Si IV is optically thin (i.e., $\tau_0 < 1$) for most of f and FWHM and for most of $\log n_e > 10$. Therefore, we cannot rule out weak absorption effects completely, but the analysis suggests that Si IV is optically thin for most of the possible flaring atmospheric conditions and suitable for an analysis of turbulence in the lower atmosphere.

Emission of Si IV 1402.77 Å under nonideal conditions
Nonequilibrium ionization

Nonequilibrium ionization effects can cause peak formation temperatures to shift by $\log T = 0.3$ K in densities of $n_e = 10^{10}\ cm^{-3}$, but the shift should be negligible for larger densities (30), and line emission can be formed over a greater height range (31). Further, Olluri et al. (32) studied C IV, an ion formed at a similar temperature to Si IV ($\log T = 5.0$) via modeling, and they suggested that temperature gradients and flow velocities can disrupt ionization equilibrium, and we might expect these conditions during a flare (e.g., chromospheric evaporation). However, this is a weak flare, and we did not see any strong evidence for large flows before and during the flare in the studied region.

Multithermal plasma

In the analysis, we assumed that the average temperature of the region is close to the peak formation temperature of Si IV, and hence, we removed the thermal broadening associated with this temperature (~80,000 K). However, Si IV, like other spectral lines, can be formed over a range of temperature. The contribution function [$G(T)$; fig. S2] shows that the emission of Si IV falls by one order of magnitude between the temperatures of 50,000 to 140,000 K, and these temperatures would cause the thermal width to only vary between 5 and 9 km/s, which is negligible compared to the observed nonthermal line broadening of 30 km/s. So, even if nonequilibrium ionization effects force Si IV to be formed at higher temperatures, this cannot account for the observed broadening (~30 km/s), and hence, the formation of Si IV in a multithermal plasma does not change the result or the interpretation of the result.

A comparison with the Mg II k line (2796.35 Å)

In this observation, Si IV 1402.77 Å was the only optically thin line suitable for the analysis. However, we can compare the temporal evolution of the Si IV 1402.77 Å centroid position with the centroid positions of another available line, the Mg II k line 2796.35 Å, formed at the cooler temperature T (K) of $\log T = 4.5$. We did not perform a detailed study of the Mg II line here, since the Mg II h and k resonance lines tend to have a double peak due to effects of reabsorption. Hence, in most formation conditions, Mg II is optically thick, and it can be formed over multiple layers in the low atmosphere, from the temperature minimum region to the upper chromosphere (33). Therefore, we can only estimate the line centroid positions (and hence relative bulk velocities) using a moment analysis. We note that the skewness (the third moment of the distribution) of the Mg II k line changes between values of (−0.1, +0.1) during flare times, and it is possible that this could affect the interpretation of the line centroid position during the flare. In fig. S3, we compared the temporal evolution and changes in centroid position for both Si IV and Mg II. The changes that we observed in the Si IV centroid position seemed to be repeated for Mg II, but to a much lesser extent. The magnitudes of the Si IV line velocities are larger with values between −18 and 5 km/s (±4 km/s) compared to the Mg II velocity range of −2 to 3 km/s. We noted that Si IV was difficult to analyze outside of the studied region, but Mg II is a stronger line in outside quiet regions. Hence, we tested whether the same changes in the Mg II centroid position were observed in different regions away from the flare, which could suggest an instrumental cause. We did not observe these centroid changes in the quiet region (fig. S3), and hence, this suggests that the changes in centroid position, and therefore also the width, are physical in this observation.

Si IV 1402.77 Å centroid and width analysis

In the main text, we analyzed the centroid position and line broadening over a spatially integrated region made up of seven pixels, in the north-south direction, from $Y = -114.9''$ to $Y = -112.9''$. We also analyzed the seven pixels that make up this region individually. Compared with the spatially integrated case, we found that each of the seven individual pixels showed a similar temporal evolution in their centroid positions and nonthermal line broadenings. In fig. S4, we showed the temporal evolution of centroid position and FWHM for two of the individual pixels: pixel 2 and pixel 4 located at $Y = -114.2''$ and $Y = -113.6''$, respectively. In all cases (Fig. 3 and fig. S4), the linewidths were determined from the second moment of the distribution, and for the Gaussian fitting, we determined the Gaussian FWHM using $2 A[3] [2\ln(2)]^{1/2}$ or as $2\sigma [2\ln(2)]^{1/2}$ from the moment analysis. The total line FWHM was given by $\text{FWHM} = [\text{FWHM}_{\text{inst}}^2 + 4\ln(2) (\lambda/c)^2 (v_{\text{th}}^2 + v_{\text{nth}}^2)]^{1/2}$, where $\text{FWHM}_{\text{inst}}$ denotes the IRIS instrumental broadening (Å), c denotes the speed of light (km/s), v_{th} (km/s) denotes the thermal Doppler velocity of the parent Si IV ions, and v_{nth} (km/s) denotes the average nonthermal velocity of the plasma, along the line of sight. We determined the nonthermal line velocity by removing the IRIS instrumental broadening with a velocity of 3.9 km/s (13) and the Si IV thermal velocity of $v = (2k_BT/M)^{1/2} = 6.86$ km/s, in quadrature, where k_B is the Boltzmann constant (erg/K), and M is the mass of the Si ion (g). The line centroid was converted to a Doppler velocity using $v = c(\lambda - \lambda_0)/\lambda_0$, where λ_0 is the centroid wavelength. The inferred centroid positions and FWHMs of Si IV in the integrated region of interest over all observation times are shown in Fig. 5.

Modeling the observed temporal trends of v_{nth} and v

To try and reproduce all IRIS observations (of bulk velocity and nonthermal velocity) together, we set up a simple model that represents the region emitting Si IV during the flare. We stress that we did not attempt to model the detailed transition region environment or the line emission itself but only the plasma motions in this region, at some angle $>0^{\circ}$ to the observer's line of sight. For this, we set up a region of extent z, parallel to the guiding magnetic field (see Fig. 4).

We then set up a wave with wavelength $\lambda(t)$, amplitude $A(t)$, and wave speed v, and these properties vary with time, t, as the wave(s) passes through the region z, causing the material to fluctuate at 90° to z. We passed either a single wave or multiple waves with different properties. The transverse velocity of wave i takes the simple form of

$$\sum_{i=1}^{N} V_i(t, z) = \sum_{i}^{N} A_i(t) \cos\left(\frac{2\pi}{\lambda_i(t)}\right)\left(z - \frac{v}{i}t\right)$$

A sum of multiple waves above represents interacting waves (possibly interacting Alfvén waves) that can form plasma turbulence and drive a cascade of wave energy to smaller and smaller wavelengths causing, e.g., electron heating in the region. The size of the region (z) emitting Si IV is unknown, so we defined the region in terms of the average fluctuation wavelength $\langle\lambda\rangle$, i.e., as $z/\langle\lambda\rangle$.

The model uses a time resolution of 1.7 s, matching the IRIS observations. At each time, we calculated the first moment and second moment of all transverse velocity fluctuations along z, which represent the bulk v and nonthermal velocities v_{nth}, respectively.

This simple modeling suggests several interesting results:

1. We can reproduce all the IRIS observations v and v_{nth} if we input a spectrum of waves ($\sim$10 different modes). If the number of

modes is too large, then we lose the detectable oscillations in v_{nth} at this time resolution. This limits the number of interacting modes that can produce the observations.

2. The input of a single wave with varying properties cannot reproduce the observations. A single fluctuation will produce noticeable and resolved oscillations in v, which is not observed with IRIS.

3. We can only reproduce the observation if $z/\langle\lambda\rangle$ is slightly less than 1 ($\sim$0.5). Situations where $z/\langle\lambda\rangle \gg 1$ seem to show large v_{nth} but negligible v, while situations where $z/\langle\lambda\rangle \ll 1$ seem to show very large v but negligible v_{nth}.

To match the observations, we required a spectrum of interacting waves, and this produces an initial transverse velocity field with greater anisotropy than a single passing wave, becoming more and more isotropic with time.

From the spectral line observations, at the start of the flare, the line profiles do show some anisotropy, but overall, they are approximately symmetrical (Fig. 2). Therefore, this suggests that the turbulence is unresolved by the IRIS observations over a single pixel distance of $\sim$240 km. However, we do not know the extent of the region emitting Si IV, along the line of sight. Again, the contribution function $G(T)$ (fig. S2) might suggest that Si IV could be formed over a temperature of 50,000 to 140,000 K, within one order of magnitude of its peak emission, and in the RADYN model atmosphere, this corresponds to a restricted height range of $\leq$100 km, at the start of the flare. Hence, if z is of the order $\leq$100 km, then the above modeling suggests that $\langle\lambda\rangle \leq$200 km. However, the location of this temperature range is dynamic as a function of height throughout the simulations, but it is generally >1.5 Mm above the canonical photosphere "surface," or middle to top chromosphere and transition region. Therefore, our back of the envelope calculations should be viewed with caution, and we stress that a more detailed study, beyond the scope of this report, is required to understand the role of waves and turbulence in the lower atmosphere during the flare. Moreover, we cannot say whether these fluctuations are generated locally in the region or they are generated and transported from another location, such as the corona, during the flare energy release process.

SUPPLEMENTARY MATERIALS

Fig. S1. A context image of the solar flare in active region 12615.
Fig. S2. Si IV contribution function.
Fig. S3. A comparison of Si IV 1402.77 Å and Mg II 2796.35 Å centroid positions.
Fig. S4. Temporal evolution of Si IV 1402.77 Å line properties during the flare (for two individual pixels).
Movie S1. Light curves and the images and line spectra of flare SOL2016-12-06T10:36:58 at all studied times during the flare rise, peak, and decay (associated with Fig. 1).
Movie S2. Plasma velocity fluctuations in space and time due to the passage of a single wave (associated with Fig. 4).
Movie S3. Plasma velocity fluctuations in space and time due to the passage of multiple interacting waves (associated with Fig. 4).

REFERENCES AND NOTES

1. T. N. Larosa, R. L. Moore, A mechanism for bulk energization in the impulsive phase of solar flares: MHD turbulent cascade. *Astrophys. J.* **418**, 912–918 (1993).
2. L. Vlahos, H. Isliker, F. Lepreti, Particle acceleration in an evolving network of unstable current sheets. *Astrophys. J.* **608**, 540–553 (2004).
3. L. Fletcher, H. S. Hudson, Impulsive phase flare energy transport by large-scale Alfvén waves and the electron acceleration problem. *Astrophys. J.* **675**, 1645–1655 (2008).
4. G. A. Doschek, U. Feldman, R. W. Kreplin, L. Cohen, High-resolution X-ray spectra of solar flares. III - General spectral properties of X1-X5 type flares. *Astrophys. J.* **239**, 725–737 (1980).

5. E. Antonucci, M. A. Dodero, Temperature dependence of nonthermal motions in solar flare plasmas observed with the flat crystal spectrometer on SMM. *Astrophys. J.* **438**, 480–490 (1995).

6. R. O. Milligan, Spatially resolved nonthermal line broadening during the impulsive phase of a solar flare. *Astrophys. J.* **740**, 70 (2011).

7. T. Kosugi, K. Matsuzaki, T. Sakao, T. Shimizu, Y. Sone, S. Tachikawa, T. Hashimoto, K. Minesugi, A. Ohnishi, T. Yamada, S. Tsuneta, H. Hara, K. Ichimoto, Y. Suematsu, M. Shimojo, T. Watanabe, S. Shimada, J. M. Davis, L. D. Hill, J. K. Owens, A. M. Title, J. L. Culhane, L. K. Harra, G. A. Doschek, L. Golub, The *Hinode* (Solar-B) mission: An overview. *Sol. Phys.* **243**, 3–17 (2007).

8. J. L. Culhane, L. K. Harra, A. M. James, K. Al-Janabi, L. J. Bradley, R. A. Chaudry, K. Rees, J. A. Tandy, P. Thomas, M. C. R. Whillock, B. Winter, G. A. Doschek, C. M. Korendyke, C. M. Brown, S. Myers, J. Mariska, J. Seely, J. Lang, B. J. Kent, B. M. Shaughnessy, P. R. Young, G. M. Simnett, C. M. Castelli, S. Mahmoud, H. Mapson-Menard, B. J. Probyn, R. J. Thomas, J. Davila, K. Dere, D. Windt, J. Shea, R. Hagood, R. Moye, H. Hara, T. Watanabe, K. Matsuzaki, T. Kosugi, V. Hansteen, Ø. Wikstol, The EUV imaging spectrometer for Hinode. *Sol. Phys.* **243**, 19–61 (2007).

9. L. K. Harra, S. Matthews, J. L. Culhane, M. C. M. Cheung, E. P. Kontar, H. Hara, The location of non-thermal velocity in the early phases of large flares—Revealing pre-eruption flux ropes. *Astrophys. J.* **774**, 122 (2013).

10. G. A. Doschek, D. E. McKenzie, H. P. Warren, Plasma dynamics above solar flare soft X-ray loop tops. *Astrophys. J.* **788**, 26 (2014).

11. E. P. Kontar, J. E. Perez, L. K. Harra, A. A. Kuznetsov, A. G. Emslie, N. L. S. Jeffrey, N. H. Bian, B. R. Dennis, Turbulent kinetic energy in the energy balance of a solar flare. *Phys. Rev. Lett.* **118**, 155101 (2017).

12. P. Goldreich, S. Sridhar, Toward a theory of interstellar turbulence. 2: Strong Alfvénic turbulence. *Astrophys. J.* **438**, 763–775 (1995).

13. B. De Pontieu, A. M. Title, J. R. Lemen, G. D. Kushner, D. J. Akin, B. Allard, T. Berger, P. Boerner, M. Cheung, C. Chou, J. F. Drake, D. W. Duncan, S. Freeland, G. F. Heyman, C. Hoffman, N. E. Hurlburt, R. W. Lindgren, D. Mathur, R. Rehse, D. Sabolish, R. Seguin, C. J. Schrijver, T. D. Tarbell, J.-P. Wülser, C. J. Wolfson, C. Yanari, J. Mudge, N. Nguyen-Phuc, R. Timmons, R. van Bezooijen, I. Weingrod, R. Brookner, G. Butcher, B. Dougherty, J. Eder, V. Knagenhjelm, S. Larsen, D. Mansir, L. Phan, P. Boyle, P. N. Cheimets, E. E. DeLuca, L. Golub, R. Gates, E. Hertz, S. McKillop, S. Park, T. Perry, W. A. Podgorski, K. Reeves, S. Saar, P. Testa, H. Tian, M. Weber, C. Dunn, S. Eccles, S. A. Jaeggli, C. C. Kankelborg, K. Mashburn, N. Pust, L. Springer, R. Carvalho, L. Kleint, J. Marmie, E. Mazmanian, T. M. D. Pereira, S. Sawyer, J. Strong, S. P. Worden, M. Carlsson, V. H. Hansteen, J. Leenaarts, M. Wiesmann, J. Aloise, K.-C. Chu, R. I. Bush, P. H. Scherrer, P. Brekke, J. Martinez-Sykora, B. W. Lites, S. W. McIntosh, H. Uitenbroek, T. J. Okamoto, M. A. Gummin, G. Auker, P. Jerram, P. Pool, N. Waltham, The *Interface Region Imaging Spectrograph* (IRIS). *Sol. Phys.* **289**, 2733–2779 (2014).

14. H. Tian, P. R. Young, K. K. Reeves, B. Chen, W. Liu, S. McKillop, Temporal evolution of chromospheric evaporation: Case studies of the M1.1 flare on 2014 September 6 and X1.6 flare on 2014 September 10. *Astrophys. J.* **811**, 139 (2015).

15. S. K. Antiochos, P. A. Sturrock, Evaporative cooling of flare plasma. *Astrophys. J.* **220**, 1137–1143 (1978).

16. L. W. Acton, J. W. Leibacher, R. C. Canfield, T. A. Gunkler, H. S. Hudson, A. L. Kiplinger, Chromospheric evaporation in a well-observed compact flare. *Astrophys. J.* **263**, 409–422 (1982).

17. J. R. Lemen, A. M. Title, D. J. Akin, P. F. Boerner, C. Chou, J. F. Drake, D. W. Duncan, C. G. Edwards, F. M. Friedlaender, G. F. Heyman, N. E. Hurlburt, N. L. Katz, G. D. Kushner, M. Levay, R. W. Lindgren, D. P. Mathur, E. L. McFeaters, S. Mitchell, R. A. Rehse, C. J. Schrijver, L. A. Springer, R. A. Stern, T. D. Tarbell, J.-P. Wuelser, C. Jacob Wolfson, C. Yanari, J. A. Bookbinder, P. N. Cheimets, D. Caldwell, E. E. Deluca, R. Gates, L. Golub, S. Park, W. A. Podgorski, R. I. Bush, P. H. Scherrer, M. A. Gummin, P. Smith, G. Auker, P. Jerram, P. Pool, R. Soufli, D. L. Windt, S. Beardsley, M. Clapp, J. Lang, N. Waltham, The *Atmospheric Imaging Assembly* (AIA) on the *Solar Dynamics Observatory* (SDO). *Sol. Phys.* **275**, 17–40 (2012).

18. R. P. Lin, B. R. Dennis, G. J. Hurford, D. M. Smith, A. Zehnder, P. R. Harvey, D. W. Curtis, D. Pankow, P. Turin, M. Bester, A. Csillaghy, M. Lewis, N. Madden, H. F. van Beek, M. Appleby, T. Raudorf, J. McTiernan, R. Ramaty, E. Schmahl, R. Schwartz, S. Krucker, R. Abiad, T. Quinn, P. Berg, M. Hashii, R. Sterling, R. Jackson, R. Pratt, R. D. Campbell, D. Malone, D. Landis, C. P. Barrington-Leigh, S. Slassi-Sennou, C. Cork, D. Clark, D. Amato, L. Orwig, R. Boyle, I. S. Banks, K. Shirey, A. K. Tolbert, D. Zarro, F. Snow, K. Thomsen, R. Henneck, A. Mchedlishvili, P. Ming, M. Fivian, J. Jordan, R. Wanner, J. Crubb, J. Preble, M. Matranga, A. Benz, H. Hudson, R. C. Canfield, G. D. Holman, C. Crannell, T. Kosugi, A. G. Emslie, N. Vilmer, J. C. Brown, C. Johns-Krull, M. Aschwanden, T. Metcalf, A. Conway, The Reuven Ramaty High-Energy Solar Spectroscopic Imager (RHESSI). *Sol. Phys.* **210**, 3–32 (2002).

19. H. P. Warren, J. W. Reep, N. A. Crump, P. J. A. Simões, Transition region and chromospheric signatures of impulsive heating events. I. Observations. *Astrophys. J.* **829**, 35 (2016).

20. J. W. Brosius, A. N. Daw, Quasi-periodic fluctuations and chromospheric evaporation in a solar flare ribbon observed by *IRIS*. *Astrophys. J.* **810**, 45 (2015).

21. N. L. S. Jeffrey, L. Fletcher, N. Labrosse, Non-gaussian velocity distributions in solar flares from extreme ultraviolet lines: A possible diagnostic of ion acceleration. *Astrophys. J.* **836**, 35 (2017).

22. K. P. Dere, E. Landi, H. E. Mason, B. C. Monsignori Fossi, P. R. Young, CHIANTI—An atomic database for emission lines. *Astron. Astrophys. Suppl. Ser.* **125**, 149–173 (1997).

23. E. Landi, P. R. Young, K. P. Dere, G. Del Zanna, H. E. Mason, CHIANTI—An atomic database for emission lines. XIII. Soft X-ray improvements and other changes. *Astrophys. J.* **763**, 86 (2013).

24. H. Achour, P. Brekke, O. Kjeldseth-Moe, P. Maltby, Observed redshifts in the solar transition region above active and quiet regions. *Astrophys. J.* **453**, 945–952 (1995).

25. L. Yan, H. Peter, J. He, H. Tian, L. Xia, L. Wang, C. Tu, L. Zhang, F. Chen, K. Barczynski, Self-absorption in the solar transition region. *Astrophys. J.* **811**, 48 (2015).

26. G. Del Zanna, M. Landini, H. E. Mason, Spectroscopic diagnostics of stellar transition regions and coronae in the XUV: AU Mic in quiescence. *Astron. Astrophys.* **385**, 968–985 (2002).

27. J. Dudík, V. Polito, E. Dzifčáková, G. Del Zanna, P. Testa, Non-maxwellian analysis of the transition-region line profiles observed by the *Interface Region Imaging Spectrograph*. *Astrophys. J.* **842**, 19 (2017).

28. M. Carlsson, R. F. Carlsson, Formation of solar calcium H and K bright grains. *Astrophys. J.* **481**, 500–514 (1997).

29. J. C. Allred, S. L. Hawley, W. P. Abbett, M. Carlsson, Radiative hydrodynamic models of the optical and ultraviolet emission from solar flares. *Astrophys. J.* **630**, 573–586 (2005).

30. S. J. Bradshaw, A numerical tool for the calculation of non-equilibrium ionisation states in the solar corona and other astrophysical plasma environments. *Astron. Astrophys.* **502**, 409–418 (2009).

31. B. De Pontieu, S. McIntosh, J. Martinez-Sykora, H. Peter, T. M. D. Pereira, Why is non-thermal line broadening of spectral lines in the lower transition region of the sun independent of spatial resolution? *Astrophys. J. Lett.* **799**, L12 (2015).

32. K. Olluri, B. V. Guddksen, V. H. Hansteen, Non-equilibrium ionization in the Bifrost stellar atmosphere code. *Astrophys. J.* **145**, 72 (2013).

33. G. S. Kerr, P. J. A. Simões, J. Qiu, L. Fletcher, IRIS observations of the Mg II h and k lines during a solar flare. *Astron. Astrophys.* **582**, A50 (2015).

34. J. E. Vernazza, E. H. Avrett, R. Loeser, Structure of the solar chromosphere. III - Models of the EUV brightness components of the quiet-sun. *Astrophys. J. Suppl.* **45**, 635–725 (1981).

Citation: N. L. S. Jeffrey, L. Fletcher, N. Labrosse, P. J. A. Simões, The development of lower-atmosphere turbulence early in a solar flare. *Sci. Adv.* **4**, eaav2794 (2018).

Science Advances

The development of lower-atmosphere turbulence early in a solar flare

N. L. S. Jeffrey, L. Fletcher, N. Labrosse and P. J. A. Simões

ARTICLE TOOLS	http://advances.sciencemag.org/content/4/12/eaav2794
SUPPLEMENTARY MATERIALS	http://advances.sciencemag.org/content/suppl/2018/12/03/4.12.eaav2794.DC1
REFERENCES	This article cites 34 articles, 0 of which you can access for free http://advances.sciencemag.org/content/4/12/eaav2794#BIBL
PERMISSIONS	http://www.sciencemag.org/help/reprints-and-permissions

Use of this article is subject to the Terms of Service